

# A simulation-based assessment of the revised NEMA NU-2 70-cm long test phantom for PET

R. D. Badawi, *Member, IEEE*, L.-E. Adam, *Member, IEEE* and R. E. Zimmerman, *Member, IEEE*

## Abstract

A 70cm long polyethylene cylinder of radius 10 cm containing an off-center line source has been suggested for the characterization of PET tomograph whole-body performance in terms of scatter fraction, sensitivity to randoms and count-rate capability. In this work we perform a series of Monte Carlo simulations of a full-ring BGO system operating in 3D mode and a full-ring sodium iodide system operating in 3D mode to determine how closely scatter fraction and NEC results from the 70 cm cylinder follow those found in anthropomorphic activity and attenuation distributions.

We find that the 70 cm cylinder measurements correctly rank-order the tomographs in terms of scatter fraction and NEC performance, but do not always accurately predict the actual scatter fractions or the peak NEC values encountered in the anthropomorphic models. Peak NEC for the phantom occurs at around double the activity concentrations which give rise to peak NEC in the anthropomorphic objects.

## I. INTRODUCTION

Scatter fraction and count rate behavior, in particular noise-equivalent count (NEC) rate capability, are important parameters used in the characterization of PET tomograph performance [1]. Until recently, the industry standard test object for measuring these parameters was a uniform cylinder of diameter 20 cm and length 19 cm filled with an aqueous solution of 18F [2,3]. However, this test object has now been changed to more accurately model the situation encountered in whole-body imaging by tomographs operating in 3D mode [4]. The new object is a polyethylene cylinder of diameter 20 cm and length 70 cm, with a line source insert placed at a radius of 4.5 cm and extending for the length of the cylinder.

In this work we used Monte Carlo simulations to compare scatter fraction measurements and NEC rates derived from the 70 cm cylinder with those derived from anthropomorphic activity and attenuation distributions for generic tomographs representative of two classes of camera design – Bismuth Germanate (BGO) ring tomographs and dedicated Sodium Iodide (NaI) ring tomographs. Only 3D mode operation was simulated.

---

R.D. Badawi is with the Division of Nuclear Medicine, Dana Farber Cancer Institute and with the Joint Program in Nuclear Medicine, Harvard Medical School, 44 Binney Street, Boston MA 02115; ramsey\_badawi@dfci.harvard.edu

L.-E. Adam is with the Department of Radiology, University of Pennsylvania, 3400 Spruce Street, Philadelphia 19104.

R.E. Zimmerman is with Department of Radiology, Brigham and Women's Hospital; Joint Program in Nuclear Medicine, Harvard Medical School, Boston, Massachusetts 02115

## II. MATERIALS AND METHODS

### A. Simulation software

The SimSET public domain software package [5] was used to perform Monte Carlo modeling of true and scattered photons arising from positron decay. Compton and photoelectric interactions were tracked within the attenuating media, detectors and end shields. Within the detector the centroid of interaction and total deposited energy were computed for each photon. Energy resolution was modeled as a Gaussian blur of recorded energy. For NaI detectors, a full-width at half-maximum (FWHM) of 12% for 511 keV photons was employed, whereas for BGO a FWHM of 20% was used. Coherent scatter, positron range and photon non-collinearity were not simulated.

### B. Tomograph construction

**Generic BGO tomograph:** The detectors were modeled as an annulus of BGO 3 cm thick, with a radius of approximately 46 cm and an axial extent of 15.2 cm. The end shields were modeled as parallel lead plates, abutting the detectors and with an inner radius of approximately 34 cm. A lower energy-level discriminator (LLD) cut-off of 350 keV was chosen, as this is the clinical setting for the HR+ BGO PET tomograph (Siemens/CTI, Knoxville, TN). For NEC calculations, factors affecting sensitivity such as detector edge effects and packing fraction were accounted for by scaling simulated true and singles rates with data acquired at low rates on a GE Advance tomograph operating in 3D mode (GE Medical Systems, Milwaukee, MI).

**Generic NaI tomograph:** The detectors were modeled as an annulus of NaI 2.54 cm thick, with a radius of 45cm and an axial length of 25.6 cm. The end shields were again modeled as parallel lead plates, abutting the detectors and with an inner radius of approximately 31 cm. For NEC calculations, factors affecting sensitivity were accounted for by scaling simulated true and singles rates with data acquired at low rates on an ADAC C-PET (ADAC-UGM, Philadelphia, PA). A lower energy-level discriminator (LLD) cut-off of 435 keV was used (the clinical setting for the C-PET).

### C. Dead time models

**Generic BGO tomograph:** We used the simple dead-time model described by Eriksson *et al* for the HR+ [6], in which the detector live-time is given by

$$Detector\_Live \approx e^{-S_i \tau_{Detector}} \quad [\text{equation 1}]$$

where  $S_i$  is the singles rate on detector segment  $i$  and  $\tau_{Detector}$  is the detector dead-time. The coincidence processing live-time is given by

$$Coinc\_Live \approx e^{-\tau_{Coinc} Coinc.Load} \quad [\text{equation 2}]$$

where

$$Coinc.Load \approx$$

$$(trues + scatter + 2 \times randoms) Detector\_Live^2$$

[equation 3]

and  $\tau_{Coinc}$  is the coincidence processing dead-time. All events depositing 125 keV or more in the detector were considered valid for the purposes of the dead-time calculations.  $\tau_{Detector}$  was set to 2.6  $\mu$ sec and  $\tau_{Coinc}$  was set to 200 nsec as described by Eriksson *et al* [6]. The tomograph was considered to be constructed of 336 detector segments, but only one dead-time factor was computed for the entire system. The trigger threshold, above which detected photons were treated as full single events for the purpose of dead time calculation, was set to 125 keV.

**Generic NaI tomograph:** A dedicated NaI PET tomograph typically uses some form of zone-triggering [7,8] whereby scintillation photons from detected events are only integrated after coincidences between (overlapping) detector zones are detected. Deriving an expression for the dead time for such a system from physical principles is not trivial. We therefore used an empirical model based on paralyzing exponentials as follows

$$System\_Live \approx e^{-\tau_1 tot\_sgls} e^{-\tau_2 tot\_sgls^2}$$

where  $tot\_sgls$  is the total recorded system singles rate in counts per second.  $\tau_1$  was set to  $1.0 \times 10^{-7}$  and  $\tau_2$  was set to  $2.7 \times 10^{-15}$ . These values gave a good fit to data obtained from a 70 cm cylinder on a CPET tomograph up to activity concentrations of approximately 0.2  $\mu$ Ci/ml. The trigger threshold was set to 370 keV.

#### D. Random coincidences

Random coincidence rates for the entire system  $R_{sys}$  were computed from the simulated total singles rates  $S_{LLD}$  falling above the lower energy level discriminator using the following formula:

$$R_{sys} = S_{LLD}^2 \tau \varphi / 2\pi \quad [\text{equation 4}]$$

where  $\varphi$  is the angle subtended at the center of the tomograph by the transaxial field of view and  $\tau$  is the coincidence time-window.  $\tau$  was set to 8 nsec and the LLD was set to 435 keV for the NaI tomograph.  $\tau$  was set to 12.5 nsec and the LLD was set to 350 keV for the BGO tomograph.

For the anthropomorphic models, the randoms were assumed to be distributed uniformly across the field of view and the random coincidence rate used to calculate NEC was obtained simply by multiplying the system randoms rate by the fraction of the field of view containing the object. The randoms correction method for the NaI tomograph was assumed to be noise-free (since the current clinical randoms correction is a simple tail-fit), while that used for the BGO tomograph was assumed to be subject to Poisson uncertainty (reflecting the currently implemented delayed coincidence channel method for randoms estimation).

#### E. Scattered coincidences

For the 70 cm cylinder, scattered coincidences were integrated over the central 24 cm of the field of view. The scatter fraction was computed by binning the scatter and trues separately, rather than by interpolating under the trues peak in projections containing both trues and scatter. For the anthropomorphic models, scatter fractions were computed by integrating the scatter only within the regions occupied by the objects.

#### F. Anthropomorphic models

Three activity and attenuation maps derived from clinical head-to-toe 18F-FDG melanoma emission and transmission scans were created (figure 1). The patient weights were 54 kg, 76 kg and 121 kg. The largest patient was scanned in two acquisitions and the reconstructed image volumes were incorporated into one for the simulation. There was some misregistration at the boundary of the two scans. The other patients were both scanned from head to toe in one sweep.

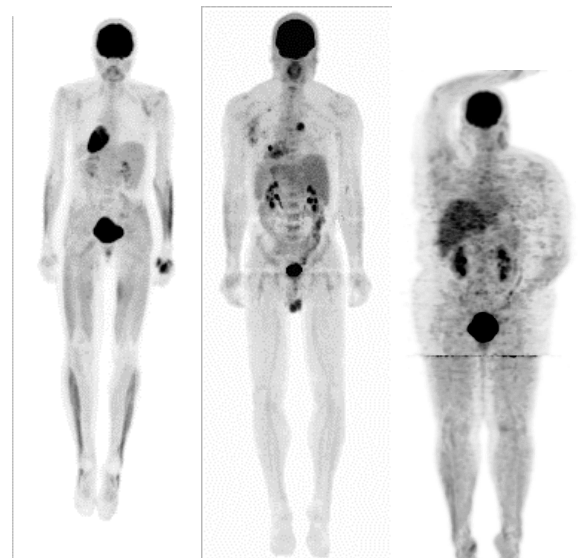


Figure 1. (left to right): 54 kg female, 76 kg male, 121 kg female. These scans were performed on an ECAT HR+ full-ring BGO scanner (Siemens/CTI, Knoxville, TN) with septa extended.

Attenuation maps for the simulations were generated by applying a simple histogram thresholding algorithm to the reconstructed transmission images, which separated the

volume into three materials corresponding to water, “lung” and air. Activity maps were generated directly from the emission images. To reduce the dynamic range of the data, activity values in the bladder were set to the mean value within the bladder. The data depth was then reduced to 256 levels per pixel and these values used to represent relative activity concentration.

A single bed position scan over the mediastinum and another immediately adjacent and superior to the bladder were simulated for each patient and for each camera geometry. Data were single-slice re-binned prior to processing.

### G. Validation measurements

NEC rates as a function of activity concentration were obtained for the ADAC CPET and the GE Advance using the 70 cm cylinder and the NEMA NU-2 2001 methodology [4]. These curves were then compared with those obtained from the generic tomograph models.

### H. Energy spectrum simulations.

In order to investigate differences between the energy distributions of photons arising from the phantom and from the anthropomorphic objects a series of simulations were carried out using tomograph models with identical geometry to those described in section IIB above, but with perfectly absorbing end shields and detectors, and with perfect energy resolution. The scattered coincidence data were binned with successively increasing lower energy levels and the resultant curves numerically differentiated with respect to energy, to yield scattered coincidence energy spectra.

## III. RESULTS

### A. Model Validation

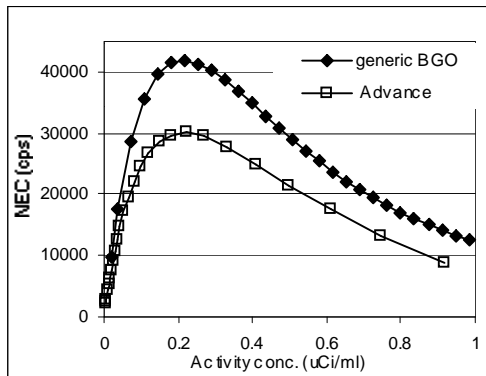


Figure 2. 70cm cylinder NEC curves for the GE Advance and for the generic BGO tomograph. Poisson noise randoms estimation was assumed.

Figures 2 and 3 show that the NEC curves for the generic tomographs are broadly similar to those computed for the CPET and the Advance. In both cases the peak NEC is greater for the generic model.

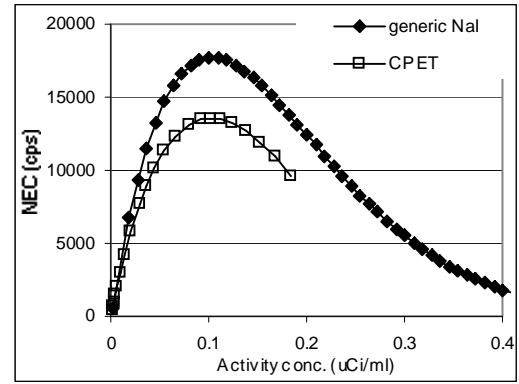


Figure 3. 70cm cylinder NEC curves for the ADAC CPET and for the generic NaI tomograph. Low-noise randoms estimation was assumed.

### B. Energy spectra

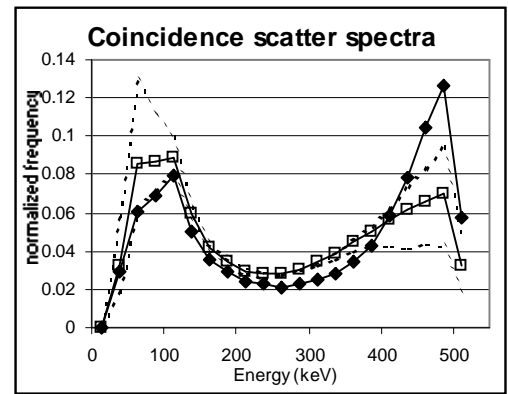


Figure 4. Mean coincidence scatter spectrum for the anthropomorphic models (open squares) and coincidence scatter spectrum for the 70 cm cylinder (solid diamonds). The range for the anthropomorphic models is shown by the dashed lines. Geometry: generic BGO tomograph.

Figure 4 shows the simulated coincidence scatter spectra obtained for the generic BGO geometry. Very similar results were obtained for the generic NaI geometry (note that ideal detectors were used for this part of the investigation). It can be seen that high-energy scatter forms a greater proportion of the total for the 70 cm phantom than it does for the anthropomorphic objects – this may reflect an increase in the likelihood of multiple scatter events in the large objects.

### C. Scatter fractions

Table 1 shows the scatter fractions for the generic scanners. The results for the 70 cm cylinder suggest that the scatter fraction for the generic NaI scanner should be less than that for the BGO scanner, and this is consistent with the anthropomorphic simulations. However, for the BGO scanner, the scatter fraction for 70 cm cylinder (0.38) is less than the mean for all conditions (0.435), whereas for

the NaI scanner, the scatter fraction for the 70 cm cylinder (0.27) is slightly more than the mean (0.262).

Position	Patient weight	Generic NaI scanner	Generic BGO scanner
70 cm cylinder	-	0.27	0.38
above bladder	54 kg	0.25	0.44
above bladder	76 kg	0.25	0.38
above bladder	121 kg	0.34	0.55
mediastinum	54 kg	0.23	0.39
mediastinum	76 kg	0.21	0.35
mediastinum	121 kg	0.29	0.50

Table 1. Scatter fractions for generic scanners.

The scatter fractions for the 76 kg male are less than those for the 54 kg female. This is probably the result of greater myocardial uptake and bladder filling in the smaller patient.

#### D. Noise-equivalent count rates

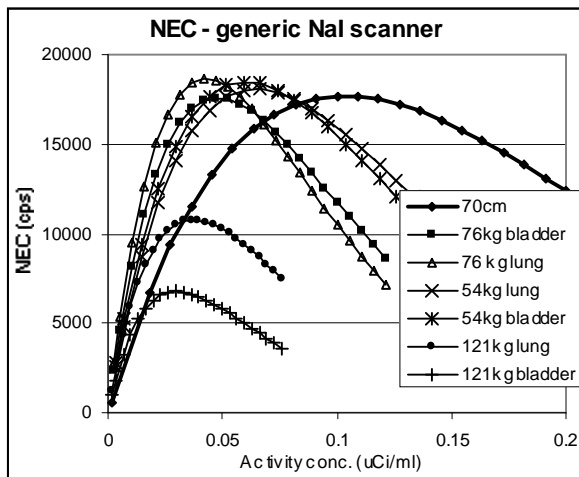


Figure 5. NEC curves for the generic Na I scanner.

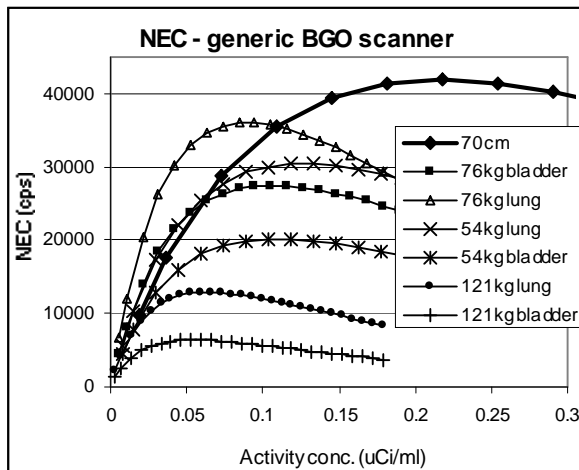


Figure 6. NEC curves for the generic BGO scanner.

Figures 5 and 6 show the NEC curves for the two generic tomographs. Activity concentrations for the 70 cm cylinder were computed by dividing the total activity in the line source by the volume of the phantom (21991 ml).

It can be seen that for the generic NaI scanner, peak NEC for the 70 cm cylinder is very similar to that found for the 54 kg and 76 kg anthropomorphic models, although unsurprisingly it is much higher than that found for the 121 kg model.

For the BGO scanner, the peak NEC for the 70 cm cylinder is greater than the highest value found in the anthropomorphic models, and is substantially higher than the average, even if the 121 kg model is excluded.

Position	Patient weight	Generic NaI scanner	Generic BGO scanner
		$\mu\text{Ci/ml}$ (mCi)	$\mu\text{Ci/ml}$ (mCi)
70 cm cylinder	-	0.10 (2.9)	0.22 ( 6.4)
above bladder	54 kg	0.059 (4.3)	0.104 ( 7.5)
above bladder	76 kg	0.047 (4.8)	0.105 (10.7)
above bladder	121 kg	0.030 (4.8)	0.053 ( 8.5)
mediastinum	54 kg	0.067 (4.8)	0.133 ( 9.6)
mediastinum	76 kg	0.042 (4.3)	0.084 ( 8.5)
mediastinum	121 kg	0.036 (5.9)	0.066 (10.7)

Table 2. Activity concentrations in  $\mu\text{Ci/ml}$  for peak NEC for generic scanners. In parentheses are total injected doses, assuming a 45 minute delay and no excretion.

Table 2 shows that in all cases, peak NEC is obtained at a higher activity concentration (although at a lower total activity) in the 70 cm cylinder than in the anthropomorphic models.

The anthropomorphic models suggest that the optimum injected dose should be about 5 mCi for the generic NaI scanner and between about 7.5 and 10 mCi for the generic BGO scanner, which is not inconsistent with current clinical practice.

#### IV. DISCUSSION AND FUTURE WORK.

Results from the 70 cm cylinder correctly rank-order the tomographs in terms of scatter fraction and NEC performance in whole-body FDG imaging.

The 70 cm cylinder data is a more accurate reflection of typical whole-body scatter fraction and peak NEC for the generic NaI tomograph than for the generic BGO tomograph, where it tends to overestimate performance. This may be due to the fact that more low-energy scatter arises from typical whole-body distributions than from the 70 cm cylinder. This scatter is preferentially rejected by the high LLD used in the generic NaI model.

The 70 cm cylinder NEC curves are not good predictors of the activity concentrations required for peak NEC in whole body imaging.

Future work should include a similar analysis of a typical dual-headed coincidence imager. This analysis could also be extended to examine simple modifications to the NEMA NU-2 2001 tests [4] to allow them to more accurately reflect whole-body performance for a range of different scanner configurations.

## V. ACKNOWLEDGEMENTS

The authors gratefully acknowledge the help of Tom Lewellen and Steve Kohlmyer (University of Washington Medical Center), who provided the measured 70cm cylinder data for the Advance.

## VI. REFERENCES

- [1] SC Strother, ME Casey and EJ Hoffman 1990 "Measuring PET Scanner Sensitivity: Relating Count rates to Image Signal-to-Noise Ratios using Noise Equivalent Counts", *IEEE Trans. Nucl. Sci.* **37**(2): 783-788
- [2] NEMA Standards Publication NU-2 1994, National Electrical Manufacturers Association, 2102 L Street, NW, Washington DC 20037-1526
- [3] International Electrotechnical Commission 1998 "EC standard 61675-1: Radionuclide Imaging Devices – Characteristics and Test Conditions – Part 1: Positron Emission Tomographs"
- [4] NEMA Standards Publication NU-2 2001, National Electrical Manufacturers Association, 2102 L Street, NW, Washington DC 20037-1526
- [5] Harrison RL, Vannoy SD, Haynor DR, Gillispie SB, Kaplan MS, and Lewellen TK "Preliminary Experience with the Photon History Generator Module of a Public-Domain Simulation System for Emission Tomography", *Conf. Rec. IEEE Nucl. Sci. Symp.*, 1154-1158, 1993.
- [6] Eriksson L, Weinhard K and Dahlbom M 1994 "A Simple Data Loss Model for Positron Camera Systems", *IEEE Trans Nucl. Sci.* **41** (4):1566-1570
- [7] Mankoff DA, Muellehner G and Miles GE 1990 "A Local Coincidence Triggering System for PET Tomographs Composed of Large-Area Position-Sensitive Detectors"
- [8] Adam LE, Karp JS, Daube-Witherspoon ME and Smith RJ. "Performance of a Whole-Body PET Scanner Using Curve-Plate NaI(Tl) Detectors" *J. Nucl. Med.*, (in press).
- [9] ME Daube-Witherspoon and G Muehllehner, 1987 "Treatment of axial data in three-dimensional PET" *J. Nucl Med.* **28**, 1717-1724